Hyperuniformity in two-dimensional periodic and quasiperiodic point patterns

Akihisa Koga[1] and Shiro Sakai[2]
[1]*Department of Physics, Tokyo Institute of Technology, Meguro, Tokyo 152-8551, Japan*
[2]*Center for Emergent Matter Science, RIKEN, Wako, Saitama 351-0198, Japan*

(Received 23 October 2023; accepted 14 March 2024; published 2 April 2024)

We study hyperuniform properties in various two-dimensional periodic and quasiperiodic point patterns. Using the histogram of the two-point distances, we develop an efficient method to calculate the hyperuniformity order metric, which quantifies the regularity of the hyperuniform point patterns. The results are compared with those calculated with the conventional running average method. To discuss how the lattice symmetry affects the order metric, we treat the trellis and Shastry-Sutherland lattices with the same point density as examples of periodic lattices, and Stampfli hexagonal and dodecagonal quasiperiodic tilings with the same point density as examples of quasiperiodic tilings. It is found that the order metric for the Shastry-Sutherland lattice (Stampfli dodecagonal tilings) is smaller than the other in the periodic (quasiperiodic) tiling, meaning that the order metric is deeply related to the lattice symmetry. Namely, the point pattern with higher symmetry is characterized by the smaller order metric when their point densities are identical. Order metrics for several other quasiperiodic tilings are also calculated.

DOI: 10.1103/PhysRevE.109.044103

I. INTRODUCTION

Quasiperiodic systems have been the subject of extensive research since the discovery of the Al-Mn quasicrystal [1]. The structures of the quasicrystals do not have the translational symmetry in the real space and are characterized by nontrivial rotation symmetries, which are forbidden in the conventional periodic lattices. Despite the aperiodicity, a quasiperiodic structure is completely ordered, leading to electron states distinct from both random and periodic systems [2–5]. However, aside from the rotational symmetry, it is not easy to capture the structural order of the quasiperiodic patterns. Hyperuniformity is a framework to quantify the degree of the order of such a point distribution in a space [6,7] and is applicable to periodic, quasiperiodic, and random systems. When the variance of the point density at a large length scale is smaller than a volume law, the system is called hyperuniform, as described later in detail. Hyperuniform point patterns are known to appear in nature, e.g., the distribution of avian photoreceptors [8] and galaxy clusters [9]. It has also been studied in applications such as photonic crystals [10–12], which has stimulated further investigations on the hyperuniform systems. It is well established that periodic and quasiperiodic point distributions exhibit hyperuniformity. The degree of the order of these point patterns can be quantified by a scalar quantity called the order metric. Then the hyperuniformity order metrics for some periodic and quasiperiodic point patterns have been studied [6,7,13–15]. Recently, electronic properties on a quasiperiodic structure have been discussed in terms of hyperuniformity [16–18]. The hyperuniformity may also be useful for characterizing the spatial distribution of the order parameter in broken-symmetry phases [19–33]. Therefore, it is instructive to give the order metrics for several periodic and quasiperiodic point patterns as references.

In this paper we study the hyperuniformity in several two-dimensional periodic and quasiperiodic lattices. We develop an efficient method to calculate the order metric precisely, exploiting the histogram of two-point distances and the filter function. We apply the method to periodic and quasiperiodic lattices composed of the squares and triangles such as Shastry-Sutherland, trellis, and hexagonal and dodecagonal Stampfli lattices [34,35]. We clarify that the point pattern with the higher rotational symmetry has a smaller order metric when the point density is identical. Furthermore, we study the effect of the depletion in the point pattern. Then we find that larger scale calculations are necessary to precisely obtain the order metric of the depleted lattices. A similar situation occurs for quasiperiodic point patterns too. We provide precisely calculated values of the order metrics for various periodic and quasiperiodic point patterns.

This paper is organized as follows. In Sec. II we briefly explain the hyperuniformity and define the order metric to characterize the regularity of the lattices. We also explain the detail of our methods to efficiently obtain the order metric. We demonstrate the benchmark of our method in Sec. III. Numerical results for various periodic and quasiperiodic lattices are shown in Sec. IV. A summary is given in the last section.

II. HYPERUNIFORMITY ORDER METRIC

In this study we focus on the hyperuniformity to characterize point patterns in two dimensions [6]. First, we consider the circular window Ω in the two-dimensional Euclidean space whose center and radius are denoted as $\mathbf{X}$ and R, respectively. The number of points inside the domain $N_{\mathbf{X}}(R)$ depends on the coordinate $\mathbf{X}$. When one examines it for sufficiently many coordinates $\mathbf{X}$, its average $\langle N_{\mathbf{X}}(R)\rangle$ is proportional to the density of points ρ, as $\langle N_{\mathbf{X}}(R)\rangle = \pi\rho(R/a)^2$, where a is the length scale of the point pattern (e.g., the distance between

neighboring points). The corresponding variance,

$$V(R) = \langle N_{\mathbf{X}}^2(R)\rangle - \langle N_{\mathbf{X}}(R)\rangle^2, \tag{1}$$

on the other hand, strongly reflects the spatial structure of the point pattern. In the large R limit, the variance may be represented as

$$V(R) = AR^2 + BR + \cdots, \tag{2}$$

with coefficients A and B. It is known that A is finite in the case of the randomly distributed point pattern [6]. By contrast, for all periodic and most of quasiperiodic point patterns, $A = 0$ and $B \neq 0$. In this case the system is called hyperuniform (class I) and the coefficient B characteristic of the point pattern is called an order metric. Notably, the condition $A = 0$ can be satisfied for not only the above-mentioned ordered point patterns, but also certain disordered point patterns, as have been discussed in Refs. [6,7]. Here we systematically examine the order metrics for various periodic and quasiperiodic lattices.

To evaluate the order metric, we define the function $\Lambda(R)$ as

$$\Lambda(R) = \frac{V(R)}{R} \tag{3}$$

for two-dimensional hyperuniform point patterns and

$$B = \lim_{R\to\infty} \Lambda(R). \tag{4}$$

In this study, we concentrate on the ordered point patterns with periodic and quasiperiodic structures, which allows us to make use of a formula, Eq. (62) in Ref. [6], obtained for a single-point configuration consisting of a large number of points in a large system volume. $\Lambda(R)$ is then given as

$$\Lambda(R) = 4\phi\left(\frac{R}{a}\right)\left[1 - 4\phi\left(\frac{R}{a}\right)^2 + \frac{1}{N}\sum_{i\neq j}\alpha(r_{ij};R)\right], \tag{5}$$

with $\phi = \pi\rho/4$, $r_{ij}(= |\mathbf{r}_i - \mathbf{r}_j|)$ the distance between ith and jth points, and

$$\alpha(r;R) = \begin{cases} \frac{2}{\pi}\left[\cos^{-1}\frac{r}{2R} - \frac{r}{2R}\left(1 - \frac{r^2}{4R^2}\right)\right] & (r \leqslant 2R) \\ 0 & (r > 2R) \end{cases}. \tag{6}$$

Note that ϕ corresponds to the packing factor F when the minimal two-point distance equals a. The sum in Eq. (5) is taken for all two points in the point pattern. This means that one can evaluate $\Lambda(R)$ without performing the samplings of the circular windows in the two-dimensional space. We note that $\bar{\Lambda}(R) = \Lambda(R)\phi^{-1/2}$ is the scale-independent function, which will be mainly discussed in the following.

In the ordered point pattern, the two-point distance r_{ij} takes certain discrete values. This allows us to introduce its histogram as

$$h(r) = \frac{1}{N}\sum_{i\neq j}\delta_{r,r_{ij}} = \sum_k \omega_k \delta_{r,r_k}, \tag{7}$$

where ω_k is the weight of the two-point distance r_k. By means of the histogram, we obtain

$$\bar{\Lambda}(R) = 2\sqrt{\pi\rho}\left(\frac{R}{a}\right)\left[1 - \pi\rho\left(\frac{R}{a}\right)^2 + \sum_k \omega_k \alpha(r_k;R)\right], \tag{8}$$

$$\psi(R) = \frac{1}{\pi}\left(\frac{a}{R}\right)^2\left[1 + \sum_k \omega_k \theta(R - r_k)\right], \tag{9}$$

where $\psi(R)$ is the average point density in the circular region centered at a point with radius R. θ is the Heaviside step function. We note that, for the periodic lattices, we evaluate the histogram $h(r)$ with a set of $\{r_k, \omega_k\}$, focusing on each inequivalent point in the unit cell and calculating the distances between it and other points in the entire space.

In both periodic and quasiperiodic point patterns, the distance between neighboring points is of the scale of a, resulting in oscillation behavior in $\bar{\Lambda}(R)$ and $\psi(R)$ in the scale of a. Nevertheless, $\psi(R)$ well converges to ρ in the limit $R \to \infty$. This may be useful to confirm the precision of the histogram. By contrast, $\bar{\Lambda}(R)$ always oscillates with respect to R. Therefore, the running (cumulative moving) average [36]

$$f_1(R) = \frac{1}{R - R_0}\int_{R_0}^{R} f(r)\,dr, \tag{10}$$

with $f = \bar{\Lambda}$ or ψ has been used to deduce the average. The constant R_0 is set to zero in this study unless otherwise mentioned. Now, we propose another way to evaluate the average as

$$f_2(R) = \frac{\int_0^\infty f(r)g(r;R)\,dr}{\int_0^\infty g(r;R)\,dr}, \tag{11}$$

where $g(r;R)$ is a filter function. If $g(r;R) = \theta(R - r)$, $f_2(R)$ is reduced to $f_1(R)$. Practically, we use the Gauss function as the filter function,

$$g(r;R) = \frac{1}{\sqrt{\pi}\sigma}\exp\left[-\left(\frac{r - R}{\sigma}\right)^2\right], \tag{12}$$

where R is the center of the Gaussian and σ is its width.

For a finite system size tractable with a numerical calculation, the running average f_1 is appropriate to roughly evaluate the order metric, but strongly depends on the endpoints of the integral since $\bar{\Lambda}$ and ψ always oscillate with respect to R. This also yields oscillation behavior in f_1, and it becomes difficult to obtain the order metric precisely. On the other hand, the Gaussian function in the filter method strongly suppresses the oscillations at the endpoints of the integral, which allows us to evaluate the order metric precisely. Furthermore, $f_2(R)$ with a finite R little depends on the local structure ($R \sim 0$) since it is evaluated with the integral around R, $(R - \sigma, R + \sigma)$, in contrast to the running average f_1 and the extrapolation method [14]. Therefore, this filter function method is expected to suppress oscillations in $\bar{\Lambda}(R)$ and $\psi(R)$, giving precise values of the averages at reasonable numerical costs, as we shall demonstrate in the following.

III. BENCHMARK OF THE METHOD

Here we perform a benchmark of our method. As a simple example, we start with a square lattice with a lattice constant a, which is shown in Fig. 1(a). Figure 1(b) shows the histogram as a function of the distance R. We see that ω_k is always a multiple of four, i.e., $\omega_k = 4m$ with integer m, reflecting the fourfold rotational symmetry. The running

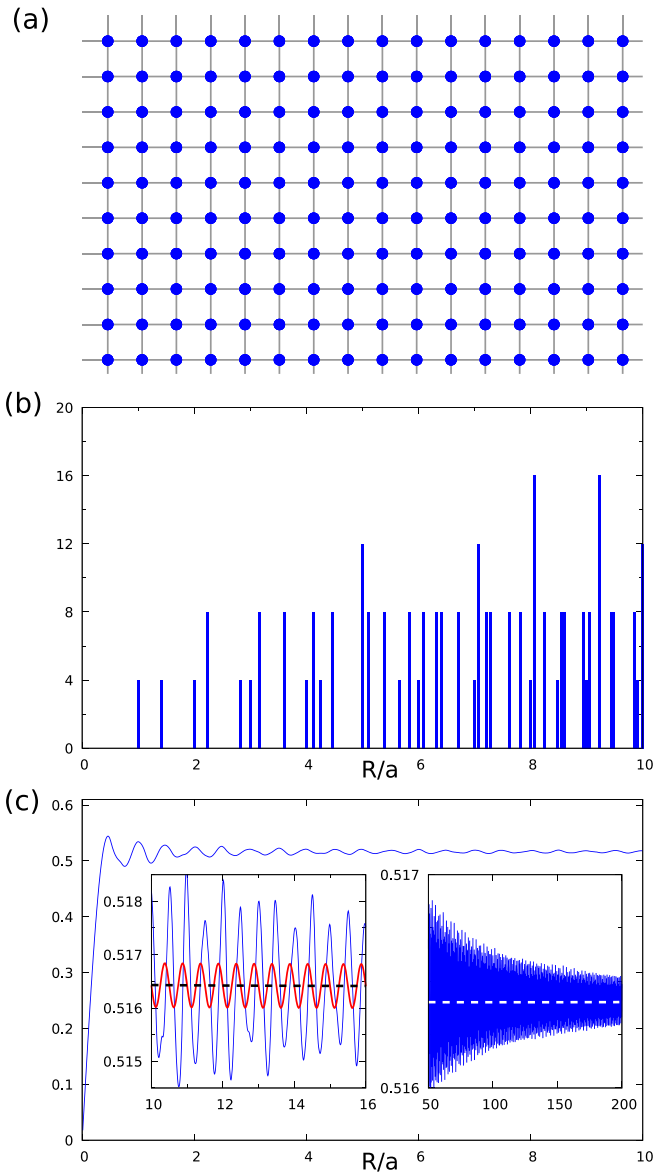

FIG. 1. (a) Square lattice and (b) its histogram $h(R)$. (c) Running average $\bar{\Lambda}_1(R)$ for the square lattice. Left inset: Thin blue curve shows the result of the running average, while red bold solid and black dashed curves indicate $\bar{\Lambda}_2(R)$ obtained by the Gaussians with $\sigma/a = 0.4$ and $\sigma/a = 2.0$, respectively. Right inset: Blue solid curve shows the running average, while white dashed line shows the result with $\sigma/a = 2.0$.

average $\bar{\Lambda}_1(R)$ is shown in Fig. 1(c). It is seen that the running average approaches a certain value for $R/a \gtrsim 2$, while oscillations remain up to a much larger R, as shown in the insets. Therefore, careful treatments are necessary to obtain the order metric precisely. We also show the results $\bar{\Lambda}_2(R)$ obtained by means of the Gaussian filter with $\sigma/a = 0.4$ and 2.0 as the bold solid and dashed curves in the left inset of Fig. 1(c). Small oscillations appear for $\sigma/a = 0.4$, while it is negligible for $\sigma/a = 2.0$. The latter result seems almost constant up to $R/a = 200$, which is shown in the right inset. This contrasts with larger oscillation behavior observed in the running average $\bar{\Lambda}_1(R)$. The results for several choices of Gaussian

TABLE I. Normalized order metric $\bar{\Lambda}_2$ and density of points ψ_2 for the square lattice obtained by means of the Gaussian filters $g(r;R)$ with R and σ.

R/a	σ/a	$\bar{\Lambda}_2$	ψ_2	R/a	σ/a	$\bar{\Lambda}_2$	ψ_2
5	0.2	0.512661	0.976985	30	1.0	0.516404	1.000000
10	0.2	0.512530	0.994516	30	5.0	0.516404	1.000000
10	0.5	0.516429	0.999149	50	5.0	0.516402	1.000000
10	1.0	0.516429	1.000000	100	5.0	0.516402	1.000000

parameters are shown in Table I. We find that the obtained values are well converged to five digits around $R/a \sim 100$ and $\sigma/a \sim 5$. The normalized order metric $\bar{B} = B\phi^{-1/2}$ is obtained as $\bar{B} \sim 0.51640$, which is in good agreement with 0.516401 obtained in the pioneering work [6]. We also note that, even with a smaller σ, reasonable results are obtained, by taking into account the width of the oscillations in $\bar{\Lambda}_2(R)$. This contrasts with the conventional running average method, whose results are shown in Table II. The less precise result originates from the fact that the quantities are strongly affected by the ends of the integral interval for the oscillation function in Eq. (10).

The quasiperiodic point pattern has unique properties distinct from the periodic and disordered patterns. One of them is the nonperiodic repeated structure in the tiling, which is known as Conway's theorem for the Penrose tiling [37,38]. In generic quasiperiodic patterns, any finite part of the point pattern repeats itself within a finite distance proportional to its diameter. Therefore, in the thermodynamic limit, the circular region with a radius R appears ubiquitously at a density $\sim O(R^{-2})$. For a circular window of radius R centered at a point, there are only a finite number of the possible point patterns inside the window, while the number increases with increasing R. Since it is hard to evaluate analytically $\{r_k, \omega_k\}$ for the large R, we here deduce the histogram by means of random sampling.

We briefly explain the details of our sampling. As discussed above, a large number of samples are necessary to deduce the order metric for the quasiperiodic tilings (while such a sampling is unnecessary for periodic point patterns). To this end, we use the inflation-deflation rule to systematically generate the point patterns around an arbitrary coordinate. In each sampling, we first choose a coordinate $\mathbf{X}$ in the squared area $L \times L$. Then we randomly choose a point $\mathbf{x}_i$ in the circular

TABLE II. Normalized order metric $\bar{\Lambda}_1$ and density of points ψ_1 for the square lattice obtained by means of the running average. The data are estimated by taking into account the width of the oscillation in the range $[R - \Delta R, R + \Delta R]$ with $\Delta R = 1$. We have used $R_0 = 4$ in the calculation of ψ to avoid the divergence at $R = 0$.

R/a	$\bar{\Lambda}_1$	ψ_1
5	0.516(5)	0.98(4)
10	0.516(2)	1.0002(7)
30	0.51645(8)	1.00000(2)
50	0.51643(5)	1.000001(7)
100	0.51641(2)	0.999998(1)

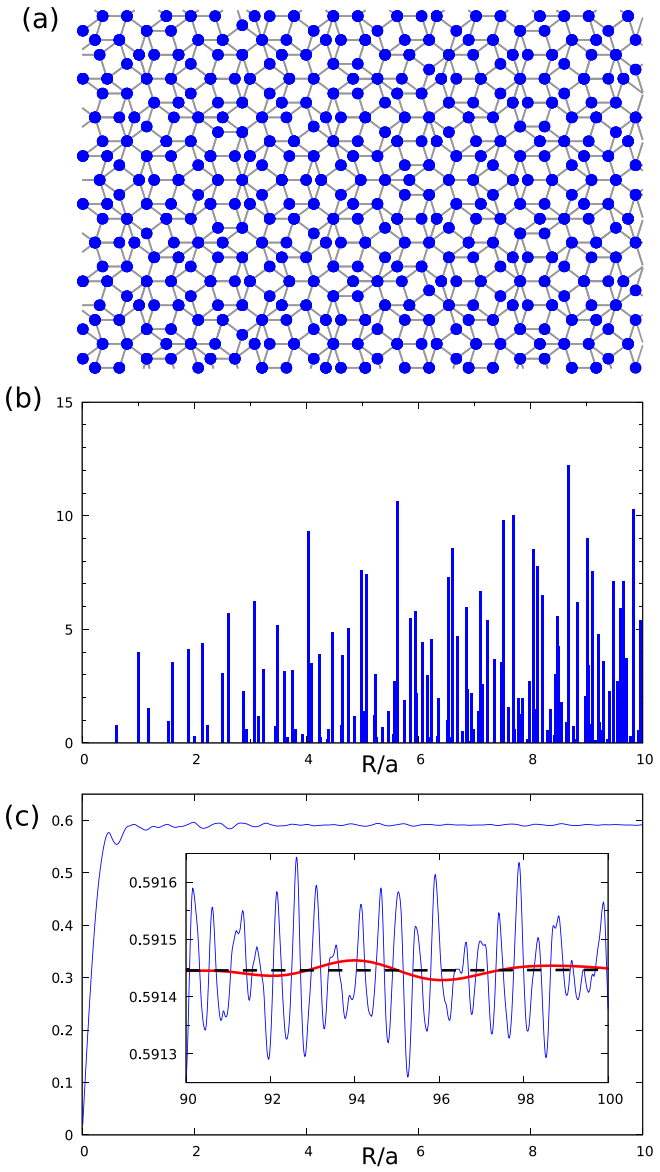

FIG. 2. (a) Penrose tiling and (b) its histogram $h(R)$. (c) The normalized running averages $\bar{\Lambda}_1(R)$ for the Penrose tiling. Red bold solid and black dashed lines in the inset represent the results $\bar{\Lambda}_2(R)$ obtained from the Gaussian filters with $\sigma/a = 2$ and $\sigma/a = 5$.

region centered at $\mathbf{X}$ with a large radius $R_{\rm samp}$. Finally, we obtain the vertices $\mathbf{x}_j$ in the circular window centered at $\mathbf{x}_i$ and calculate the set $\{r_j, \omega_j\}$ with $r_j = |\mathbf{x}_i - \mathbf{x}_j|$. Sampling many times $N_{\rm samp}$, we obtain the histogram $h(r)$. We note that the large number of samples is necessary to evaluate $\bar{\Lambda}(R)$ for large R since the number of different distances, $|\mathbf{x}_i - \mathbf{x}_j|$, is large and the fraction of each distance is tiny. Moreover, the convergence against R strongly depends on the quasiperiodic tilings. In the following we set $L = 10^8 a$, $R_{\rm samp}/a = 4000$, and $N_{\rm samp} > 10^9$.

Here we demonstrate the results for the Penrose tiling as an example of the quasiperiodic tilings, which is shown in Fig. 2(a). This tiling is composed of the skinny and fat rhombuses with edge length a. Figure 2(b) shows the histogram of Penrose tiling. This is in good agreement

TABLE III. Normalized order metric $\bar{\Lambda}_2$ and the point density ψ_2 of the Penrose tiling, obtained by means of the Gaussian filters $g(r; R)$ with the listed R/a and σ/a.

R/a	σ/a	$\bar{\Lambda}_2$	ψ_2	R/a	σ/a	$\bar{\Lambda}_2$	ψ_2
5	0.2	0.57962	1.23405	30	1.0	0.59156	1.23107
10	0.2	0.60501	1.23554	30	5.0	0.59145	1.23107
10	0.5	0.59341	1.23166	50	5.0	0.59145	1.23107
10	1.0	0.59162	1.23109	100	5.0	0.59144	1.23107

with the analytical results for small R, $(R_k/a, \omega_k) = (1/\tau, 2/\tau^2), (1, 4), (\sqrt{3-\tau}, 4/\tau^2), (\sqrt{3-1/\tau}, 4/\tau^3), (\tau, 2+4/\tau^2), (\sqrt{\tau+2}, 4+2/\tau^6), (2, 2/\tau^4)$ with the golden ratio $\tau[= (1+\sqrt{5})/2]$. We find that the number of peaks in the histogram is much larger than that for the square lattice, as discussed before. The running average approaches a certain value around $R/a \sim 2$, while it oscillates around $\bar{\Lambda}_1(R) \sim 0.6$, as shown in Fig. 2(c). The results obtained by means of the Gaussian filters with $\sigma/a = 2$ and 5 are shown as the solid and dashed curves in the inset. Invisible oscillations appear in the results with $\sigma/a = 5$. The numerical results for some sets of $\{R, \sigma\}$ are shown in Table III. We find that the obtained values are well converged to five digits around $R/a \sim 100$ and $\sigma/a \sim 5$, and are better than the results obtained by the running average shown in Table IV, similarly to the case of the square lattice. We obtain the order metric $\bar{B} \sim 0.59145$. This is smaller than the result $\bar{B} = 0.60052$ in Ref. [13], but is consistent with the recent result [14].

IV. NUMERICAL RESULTS

A. Periodic point patterns

We first show the order metrics for the square, triangular, honeycomb, and kagome lattices as simple periodic lattices. Combining the histogram and filter function methods, we obtain the results shown in Table V. Here we have set a as a distance between the nearest neighbor point pairs. These are in a good agreement with those in the pioneering works [6,13], except for that for the honeycomb lattice.

Next, we discuss how the order metric is affected by the rotational symmetry. To this end we consider the trellis and Shastry-Sutherland lattices, which are both composed of the

TABLE IV. Normalized order metric $\bar{\Lambda}_1$ and density of points ψ_1 for the Penrose tiling obtained by means of the running average. The data are estimated by taking into account the width of the oscillation in the range $[R - \Delta R, R + \Delta R]$ with $\Delta R = 1$. We have used $R_0 = 4$ in the calculation of ψ to avoid the divergence at $R = 0$.

R/a	$\bar{\Lambda}_1$	ψ_1
5	0.592(3)	1.19(7)
10	0.592(2)	1.2323(5)
30	0.5916(6)	1.23139(2)
50	0.5914(2)	1.231250(6)
100	0.5914(1)	1.231159(1)

TABLE V. Densities of points ρ, $\phi(=\pi\rho/4)$, and normalized order metrics $\bar{B}$ for various periodic point patterns.

Pattern	ρ		ϕ	$\bar{B}$
Triangular	$2/\sqrt{3}$	1.154701	0.906900	0.50835
Square	1	1.000000	0.785398	0.51640
Honeycomb	$4/(3\sqrt{3})$	0.769800	0.604600	0.56699
Kagome	$\sqrt{3}/2$	0.866025	0.680175	0.58699
1/5-depleted square	4/5	0.800000	0.628319	0.60462
Shastry-Sutherland	$8-4\sqrt{3}$	1.071797	0.841787	0.51664
Trellis	$8-4\sqrt{3}$	1.071797	0.841787	0.51877

triangles and squares with the edge length a. The latter is also known as the σ phase in metallurgy. The lattice structures are schematically shown in Figs. 3(a) and 3(b). The quantum spin systems on these lattices are known as geometrically frustrated systems, and theoretical and experimental studies have been done [39–45] in which distinct magnetic properties are discussed. From the structural point of view, in both lattices the volumes V of a Voronoi cell, atomic packing factor F, and densities of triangles and squares are identical: $V/a^2 = 1/\rho = (2+\sqrt{3})/4$, $f = \pi/(2+\sqrt{3})$, $\rho_\triangle = 2/3$, and $\rho_\square = 1/3$. This allows us to discuss how the symmetry of the point pattern affects the order metric in the absence of a trivial contribution from a change of V, F, and ρ. Namely, the point pattern of the trellis lattice belongs to the D_2 point group, while that of the Shastry-Sutherland lattice belongs to the C_4 point group.

As shown in Figs. 3(a) and 3(b), each point is shared by two squares and three triangles. Therefore, no difference appears in the histogram for $R/a < \sqrt{3}$: $(R/a, \omega) = (1, 5)$ and $(\sqrt{2}, 2)$, as shown in Fig. 3(c). On the other hand, the difference appears in the coordination number for the third nearest neighbor with a distance $R/a = \sqrt{3}$, namely, $\omega = 1$ for the Shastry-Sutherland lattice, while $\omega = 2$ for the trellis lattice. Beyond $R/a = \sqrt{3}$, a finite weight appears at a fewer values of R in the Shastry-Sutherland lattice, which reflects the higher rotational symmetry. Then $\bar{\Lambda}(R)$ and its running average for both lattices are identical for $R/a < \sqrt{3}/2$ and move apart beyond it, as seen in Fig. 3(c). Finally, we clearly find that $\bar{\Lambda}_1(R)$ takes distinct values around $R/a = 100$. The results obtained by the filter function method with $\sigma/a = 5$ are shown as the dashed lines in the inset of Fig. 3(c). The invisible oscillations appear, and we obtain $\bar{B} = 0.51664$ for the Shastry-Sutherland lattice and $\bar{B} = 0.51877$ for the trellis lattice (see Table V). This result may be explained by the difference of the rotational symmetry of the point patterns, namely, the rotational symmetry for the Shastry-Sutherland lattice is higher than the other, resulting in the smaller order metric, i.e., higher regularity.

We also discuss how the order metric is affected by the depletion in the lattice. To this end we deal with the triangular and square lattices, and consider their depleted lattices. The honeycomb and kagome lattices can be regarded as the 1/3- and 1/4-depleted triangular lattices, respectively. The kagome and 1/5-depleted square lattices are schematically shown in Figs. 4(a) and 4(b), respectively. The running averages for

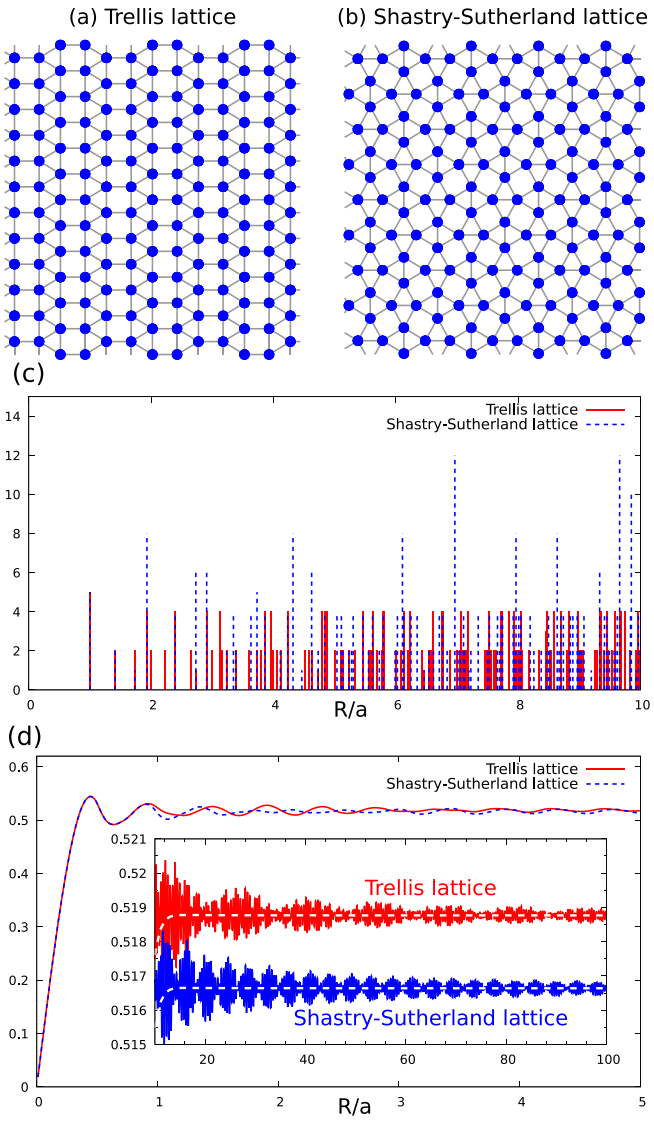

FIG. 3. (a) Trellis and (b) Shastry-Sutherland lattices and (c) their histograms. (d) Solid (dashed) lines represent the running average $\bar{\Lambda}_1(R)$ for the trellis (Shastry-Sutherland) lattice. In the inset we compare the running averages $\bar{\Lambda}_1(R)$ (solid lines) and $\bar{\Lambda}_2(R)$ (dashed lines) with $\sigma/a = 5$.

$R/a < 6$ are shown in Figs. 4(c) and 4(d). We find that the running averages for triangular and square lattices increase rapidly for $R/a \lesssim 0.5$ and tend to converge to certain values with decaying oscillation. By contrast, the running averages for the depleted lattices tend to slowly increase with oscillation even for a larger R. The amplitude of the oscillation looks larger for the depleted lattices. Thus, introducing the depletion (space) into the lattice, the running average slowly increases with R, and it becomes more difficult to precisely evaluate the order metric. This observation is important for considering the results for quasiperiodic tilings since they are composed of multiple tiles with distinct areas. By means of the filter functions with $\sigma/a = 1.0$, we obtain the smooth curves shown as the dashed lines in Figs. 4(c) and 4(d). The order metrics for the above depleted lattices are shown as the diamonds and in Table V.

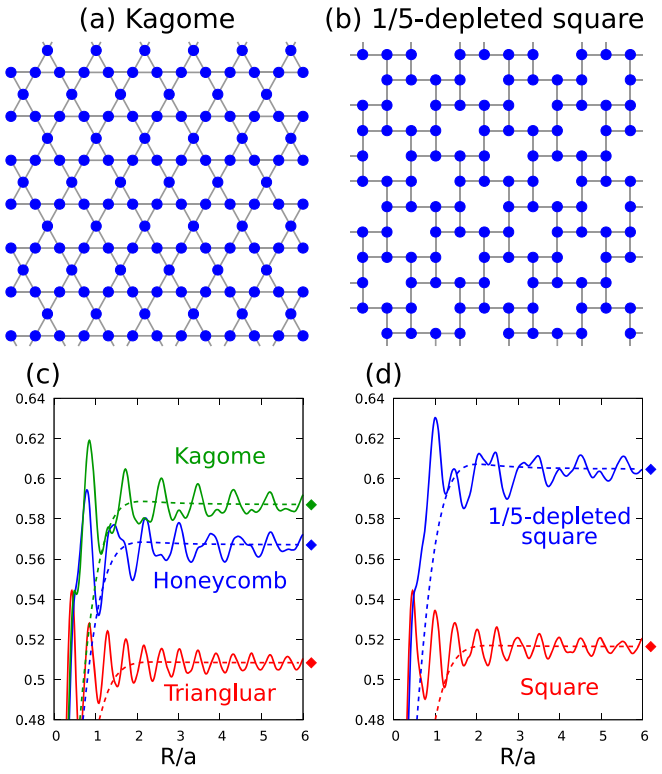

FIG. 4. (a) Kagome and (b) 1/5-depleted square lattices. (c) [(d)] Solid lines represent the running averages $\bar{\Lambda}_1(R)$ for the kagome, honeycomb, and triangular lattices (1/5-depleted square and square lattices) for $R/a \leqslant 6$. Dashes lines represent $\bar{\Lambda}_2(R)$ with $\sigma/a = 1.0$, and diamonds represent the normalized order metrics $\bar{B}$ shown in Table V.

B. Quasiperiodic point patterns

We next consider several quasiperiodic point patterns. First, we deal with the Stampfli hexagonal and dodecagonal tilings [34,35] composed of the triangles and squares with edge length a, which are shown in Figs. 5(a) and 5(b). These tilings are similar to each other, but a difference appears in the hexagonal structure composed of six adjacent triangles, which are shown as shaded areas in Figs. 5(a) and 5(b). Namely, two edges of each hexagon are always parallel to the y axis for the Stampfli hexagonal tilings, but the other equally includes two hexagonal structures with distinct directions. This difference hardly affects local properties but leads to the difference in the global rotational symmetry. In fact, no difference appears in the histogram for $R/a < \sqrt{3}$: $(R/a, \omega) = (1, 5 + 1/\tau_D^2)$ and $(\sqrt{2}, 4 - 8/\tau_D)$ where $\tau_D (= 2 + \sqrt{3})$ is the characteristic ratio of these tilings. On the other hand, the difference appears in the weights for the third nearest neighbor with a distance $R/a = \sqrt{3}$, namely, $\omega = 58/\tau_D - 14 \sim 1.54105$ for the hexagonal tiling, while $\omega = 33/\tau_D - 3 \sim 1.42116$ for the dodecagonal tiling. This difference is relatively smaller than that between the Shastry-Sutherland and trellis lattices discussed above. In addition, even for $R/a \gtrsim \sqrt{3}$, the locations of the peaks are almost the same and their weights take similar values, as shown in Fig. 5(c). This should lead to only a slight difference in their order metrics. Figure 5(d) shows the running averages for both tilings. When $R/a < \sqrt{3}/2$, the curves

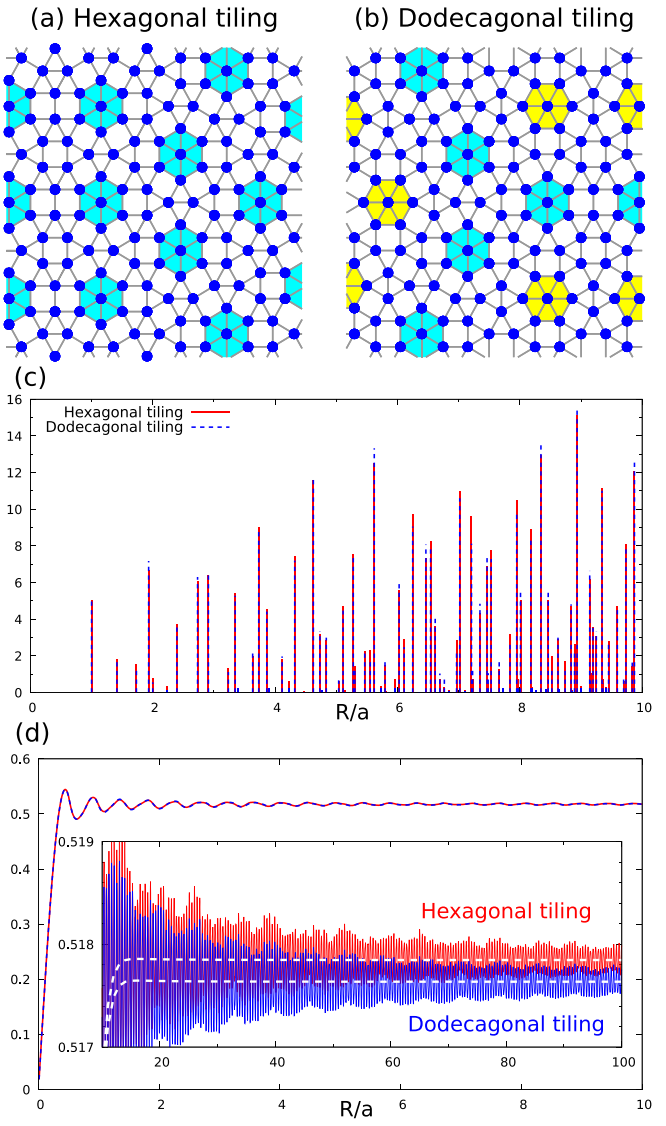

FIG. 5. (a) Stampfli hexagonal and (b) dodecagonal tilings and (c) their histograms. (d) Solid (dashed) lines represent the running average $\bar{\Lambda}_1(R)$ for the Stampfli hexagonal (dodecagonal) tiling. In the inset we compare the running averages $\bar{\Lambda}_1(R)$ (solid lines) and $\bar{\Lambda}_2(R)$ (dashed lines) with $\sigma/a = 5$.

of the running average are identical. Furthermore, a difference in these curves is invisible for $R/a < 10$. On the other hand, around $R/a = 100$, we find that the running average for the dodecagonal tiling is smaller than the other. By means of the filter function with $\sigma/a = 5$, we obtain $\bar{\Lambda}_2(R)$ for both tilings, which are shown as the dashed lines in the inset of Fig. 5(d). We hardly find oscillation behavior in $\bar{\Lambda}_2(R)$ for both tilings, and obtain the order metrics $\bar{B} = 0.51785$ for the hexagonal tiling and $\bar{B} = 0.51764$ for the dodecagonal tiling (also see Table VI). The quasiperiodic point pattern with the higher rotational symmetry has a smaller order metric, similar to the results for the periodic point patterns discussed in the previous section.

Next, we consider the Niizeki-Gähler [46,47] and Socolar [48] tilings, as examples of dodecagonal tilings. These are shown in Figs. 6(a) and 6(b). The former is composed

TABLE VI. Densities of points ρ, packing factor F, and normalized order metric $\bar{B}$ for various quasiperiodic point patterns with n-fold rotational symmetry. $\tau[=(1+\sqrt{5})/2]$ is the golden ratio, $\tau_s(=1+\sqrt{2})$ is the silver ratio, and $\tau_D(=2+\sqrt{3})$ is the ratio characteristic of the dodecagonal tilings.

Point pattern	n	ρ		F		$\bar{B}$
Square Fibonacci tiling	4	$\tau^2/5$	0.52361	$\pi\tau^2/20$	0.41124	0.835(5)
Hexagonal three-tile tiling	6	$8\tau/(15\sqrt{3})$	0.49823	$2\pi\tau/(15\sqrt{3})$	0.39131	1.39(3)
Stampfli hexagonal tiling	6	$\tau_D/(2\sqrt{3})$	1.07735	$\pi\tau_D/(8\sqrt{3})$	0.84615	0.51785
Ammann-Beenker tiling	8	$\tau_s/2$	1.20711	$\pi/(4\sqrt{2})$	0.55536	0.590(1)
Penrose tiling	10	$2\times 5^{-3/4}\tau^{3/2}$	1.23107	$5^{-3/4}\pi/(2\tau^{1/2})$	0.36932	0.59145
Stampfli dodecagonal tiling	12	$\tau_D/(2\sqrt{3})$	1.07735	$\pi\tau_D/(8\sqrt{3})$	0.84615	0.51764
Niizeki-Gähler tiling	12	$2/\sqrt{3}$	1.15470	$\pi/(2\sqrt{3}\tau_D)$	0.24300	0.599(2)
Socolar dodecagonal tiling	12	$2(3+\sqrt{3})/9$	1.05157	$(3-\sqrt{3})\pi/18$	0.22130	0.88(1)

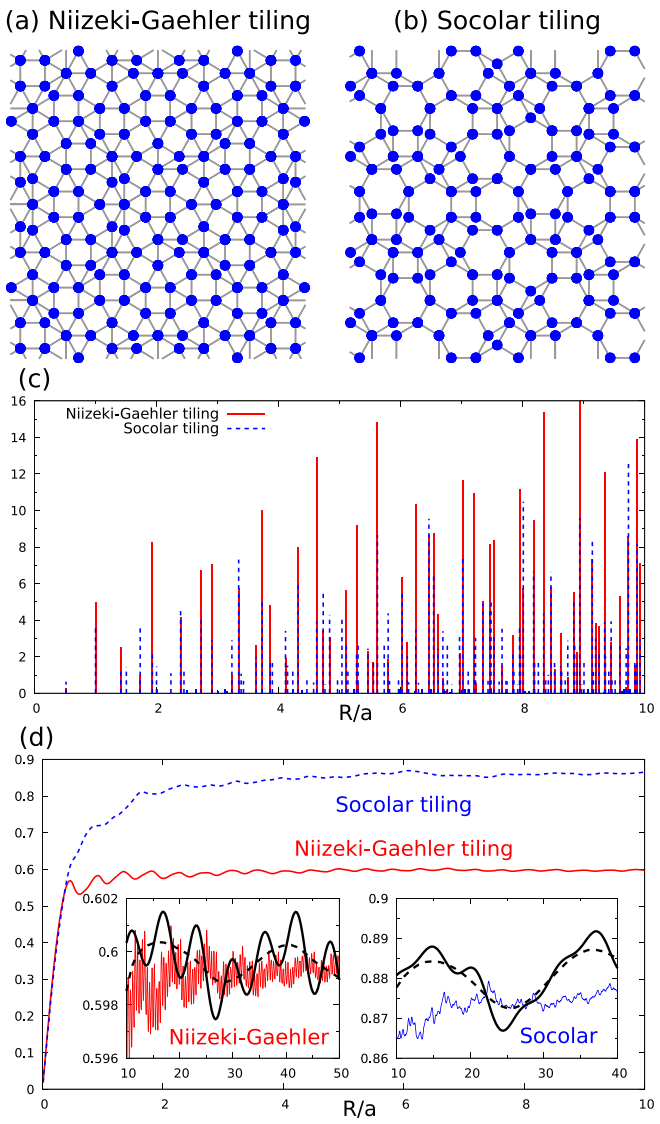

FIG. 6. (a) Niizeki-Gähler and (b) Socolar tilings and (c) their histograms. (d) Solid (dashed) lines represent the running average $\bar{\Lambda}_1(R)$ for the Niizeki-Gähler (Socolar) dodecagonal tiling. Left and right insets show the results for Niizeki-Gähler and Socolar tilings in the larger R case. Thin solid line represents the running average $\bar{\Lambda}_1(R)$, and black bold solid (dashed) line represents $\bar{\Lambda}_2(R)$ with $\sigma/a=3$ ($\sigma/a=5$).

of squares, triangles, and rhombuses. It is known that this tiling is a key structure for the two-dimensional oxide quasicrystals derived from $BaTiO_3$ and $SrTiO_3$ on a Pt(111) substrate [49,50], and structural properties have been discussed [51]. The Socolar dodecagonal tiling is composed of squares, rhombuses, and hexagons, and thereby the vertex system is bipartite. Its magnetic properties have been discussed [30,52]. As shown in Figs. 6(a) and 6(b), the vertices in the Niizeki-Gähler tiling look densely distributed, compared with the vertices in the Socolar tiling. Therefore, the weights in the histogram for the Niizeki-Gähler tiling are significantly higher than the others at particular distances, as shown in Fig. 6(c). This should affect the convergence of the running averages $\bar{\Lambda}_1(R)$. Figure 6(d) shows the running averages for both tilings. The running average for the Niizeki-Gähler tiling oscillates around 0.6 for $R/a>2$. By means of the filter function method with $\sigma/a=5$, we obtain $\bar{\Lambda}_2(R)$, which are shown as the dashed lines in the insets. In contrast to the cases of Penrose and Stampfli tilings, we find larger oscillations in $\bar{\Lambda}_2(R)$. This means that the Gaussian filter with a larger σ will be necessary to precisely evaluate the order metric although it is hard to obtain the histogram for large R due to its large computational cost. A less accurate order metric is obtained as $\bar{B}\sim 0.599(2)$, by taking into account the width of the oscillation in $\bar{\Lambda}_2(R)$. Figure 6(d) shows that the running average for the Socolar tiling slowly increases even when $R/a\gtrsim 5$. In the right inset of Fig. 6(d), a fairly large oscillation appears in $\bar{\Lambda}_2(R)$, and $\bar{\Lambda}_2(R)$ is larger than $\bar{\Lambda}_1(R)$ in most of the range ($R/a<40$). This should be explained by the following. In the tiling, there is the wide space in each hexagon and points are unevenly concentrated around rhombuses. This short-range uneven distribution leads to the slow increase in $\bar{\Lambda}(R)$ for small R, which strongly affects the running average with larger R. We then obtain the less accurate order metric $\bar{B}\sim 0.88(1)$, taking into account oscillation behavior in $\bar{\Lambda}_2(R)$.

Here we have examined the hyperuniformity for three dodecagonal tilings and have found the Stampfli, Niizeki-Gähler, and Socolar dodecagonal tilings in descending order of order metric. This result suggests that the order metric is correlated with the packing factor rather than the density of points since the Niizeki-Gähler and Socolar tilings include the rhombuses with acute angles of $\pi/6$ and their packing factors are less than that of the Stampfli tiling. The density of points ρ,

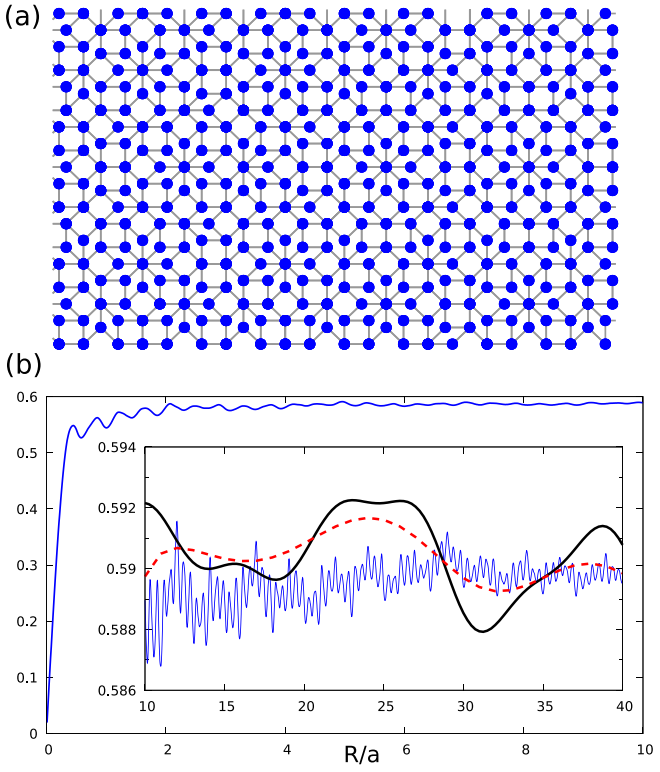

FIG. 7. (a) Ammann-Beenker tiling. (b) Thin solid line represents the running average $\bar{\Lambda}_1(R)$, and the bold solid (dashed) line represents $\bar{\Lambda}_2(R)$ obtained by the Gaussian with $\sigma/a = 3$ ($\sigma/a = 5$).

packing factor F, and normalized order metric $\bar{B}$ for several quasiperiodic tilings are explicitly shown in Table VI.

We also study the Ammann-Beenker tiling [48,53], as shown in Fig. 7(a). This tiling is composed of the squares and rhombuses and is invariant under eightfold rotation operations. Figure 7(b) shows the running average as a function of R/a, where a is the edge length of the tiles. We find that the running average seems to converge for $R/a \sim 3$ while the sampling number dependence appears in the large R region (not shown), which is similar to that for the Niizeki-Gähler and Socolar tilings discussed above. It is not so clear why the convergence of the histogram strongly depends on the tilings. By means of the filter functions, we obtain the order metrics $\bar{B} = 0.590(1)$ for the Ammann-Beenker tiling, which is smaller than that in previous work [13].

Finally, we consider the quasiperiodic tilings with two length scales and examine the order metrics for the point patterns. One of the simplest tilings is the squared Fibonacci tiling [54], where the one-dimensional Fibonacci sequences are loaded into the edges of the square lattice in both horizontal and vertical directions, as shown in Fig. 8(a). The tiling is composed of the small and large squares and rectangles. The ratio between short and long edges is set as the golden ratio. Recently, the hexagonal three-tile tiling, which is composed of small and large hexagons and parallelograms, has been found [55]. The ratio between the short and long edges is given by the golden ratio. Figure 8(c) [(d)] shows the running average for square Fibonacci (hexagonal three-tile) tiling. Similar to the Ammann-Beenker, Niizeki-Gähler, and Socolar

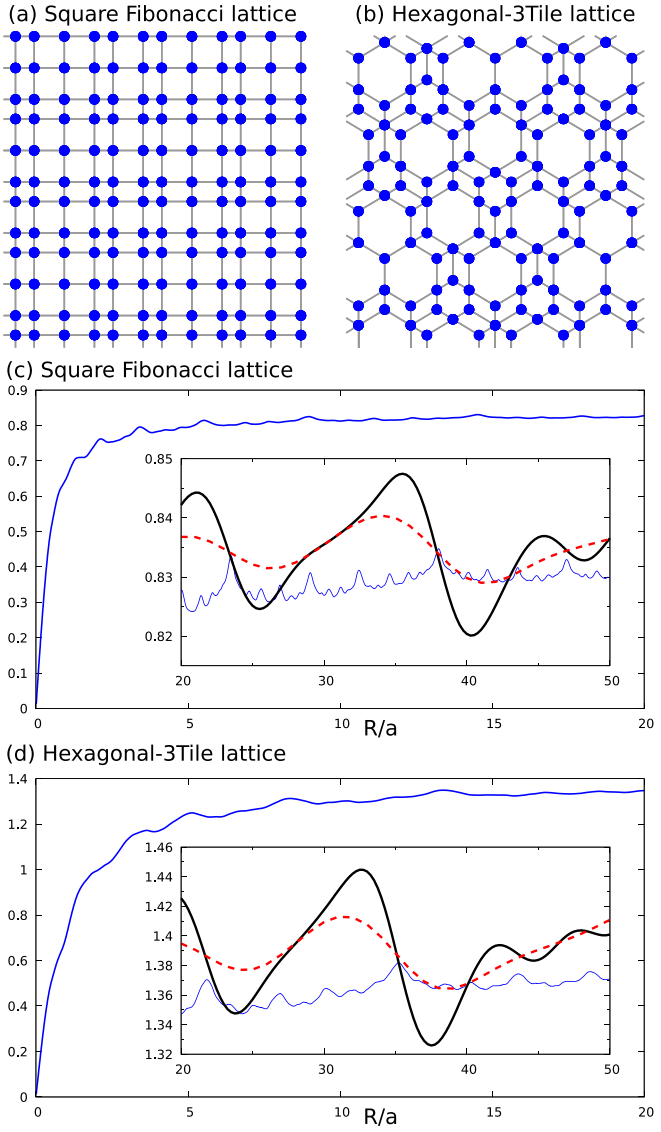

FIG. 8. (a) Square Fibonacci and (b) hexagonal three-tile lattices. (c) [(d)] Blue thin curve shows the running average for the square Fibonacci (hexagonal three-tile) lattice. Bold solid (dashed) curves in the insets of (c) and (d) represent $\bar{\Lambda}_2(R)$ obtained by the Gaussian with $\sigma/a = 3$ ($\sigma/a = 5$).

tilings, the running averages slowly increase, in contrast to the Penrose and Stampfli tilings. We obtain $\bar{B} = 0.835(5)$ for the square Fibonacci tiling and $\bar{B} = 1.39(3)$ for the hexagonal three-tile tiling by means of the filter function method with $\sigma/a = 5$.

V. SUMMARY

We have studied the hyperuniformity of the two-dimensional periodic and quasiperiodic point patterns systematically. To calculate the hyperuniformity order metric, which quantifies the regularity of the hyperuniform point patterns, we have developed an efficient method, where the filter function and histogram of two-point distances are combined. Then we have calculated the hyperuniformity order metric. For the Shastry-Sutherland and trellis lattices composed of triangles

and squares, we have demonstrated that the order metric for the former is smaller than the latter. We have also compared the order metrics for the Stampfli hexagonal and dodecagonal quasiperiodic tilings. The order metric for the former is larger than the latter. These results indicate that the order metric is deeply related to the lattice symmetry, i.e., being smaller for a higher symmetry, in addition to the density of points. The filter-function method proposed here will also be applicable to heterogeneous media consisting of discrete phases [13,56] and density (scalar-field) distributions [57]: hyperuniform density distributions appear in electron systems on quasiperiodic lattices [17,18]. Since the system size tractable with numerical simulations is limited, the method may be particularly useful in computing the order metric of such distributions.

We note that the histogram obtained within a relatively small R can give a reasonable value of the order metric. In the cases of square lattice and Penrose tiling, the order metrics to three digits are obtained from the data with $R/a \lesssim 10$, as shown in Tables I and III. This fact would be useful in evaluating the order metric for small point patterns observed in experiments.

ACKNOWLEDGMENTS

We would like to thank N. Fujita, T. Ishimasa, and T. Yamada for valuable discussions. Parts of the numerical calculations were performed on the supercomputing systems at ISSP, the University of Tokyo. This work was supported by Grant-in-Aid for Scientific Research from JSPS, KAKENHI Grants No. JP22K03525, No. JP21H01025, and No. JP19H05821 (A.K.) and No. JP22H04603 (S.S.).

[1] D. Shechtman, I. Blech, D. Gratias, and J. W. Cahn, Phys. Rev. Lett. **53**, 1951 (1984).
[2] M. Kohmoto and B. Sutherland, Phys. Rev. B **34**, 3849 (1986).
[3] B. Sutherland, Phys. Rev. B **34**, 3904 (1986).
[4] M. Kohmoto, B. Sutherland, and C. Tang, Phys. Rev. B **35**, 1020 (1987).
[5] M. Arai, T. Tokihiro, T. Fujiwara, and M. Kohmoto, Phys. Rev. B **38**, 1621 (1988).
[6] S. Torquato and F. H. Stillinger, Phys. Rev. E **68**, 041113 (2003).
[7] S. Torquato, Phys. Rep. **745**, 1 (2018).
[8] Y. Jiao, T. Lau, H. Hatzikirou, M. Meyer-Hermann, J. C. Corbo, and S. Torquato, Phys. Rev. E **89**, 022721 (2014).
[9] O. H. E. Philcox and S. Torquato, Phys. Rev. X **13**, 011038 (2023).
[10] M. Florescu, S. Torquato, and P. J. Steinhardt, Proc. Natl. Acad. Sci. USA **106**, 20658 (2009).
[11] M. Florescu, S. Torquato, and P. J. Steinhardt, Phys. Rev. B **80**, 155112 (2009).
[12] W. Man, M. Florescu, E. P. Williamson, Y. He, S. R. Hashemizad, B. Y. C. Leung, D. R. Liner, S. Torquato, P. M. Chaikin, and P. J. Steinhardt, Proc. Natl. Acad. Sci. USA **110**, 15886 (2013).
[13] C. E. Zachary and S. Torquato, J. Stat. Mech. (2009) P12015.
[14] C. Lin, P. J. Steinhardt, and S. Torquato, J. Phys.: Condens. Matter **29**, 204003 (2017).
[15] E. C. Oğuz, J. E. S. Socolar, P. J. Steinhardt, and S. Torquato, Phys. Rev. B **95**, 054119 (2017).
[16] J. N. Fuchs, R. Mosseri, and J. Vidal, Phys. Rev. B **100**, 125118 (2019).
[17] S. Sakai, R. Arita, and T. Ohtsuki, Phys. Rev. B **105**, 054202 (2022).
[18] S. Sakai, R. Arita, and T. Ohtsuki, Phys. Rev. Res. **4**, 033241 (2022).
[19] A. Jagannathan and H. J. Schulz, Phys. Rev. B **55**, 8045 (1997).
[20] S. Wessel, A. Jagannathan, and S. Haas, Phys. Rev. Lett. **90**, 177205 (2003).
[21] A. Koga and H. Tsunetsugu, Phys. Rev. B **96**, 214402 (2017).
[22] S. Sakai, N. Takemori, A. Koga, and R. Arita, Phys. Rev. B **95**, 024509 (2017).
[23] R. N. Araújo and E. C. Andrade, Phys. Rev. B **100**, 014510 (2019).
[24] S. Sakai and R. Arita, Phys. Rev. Res. **1**, 022002(R) (2019).
[25] Y. Cao, Y. Zhang, Y.-B. Liu, C.-C. Liu, W.-Q. Chen, and F. Yang, Phys. Rev. Lett. **125**, 017002 (2020).
[26] K. Inayoshi, Y. Murakami, and A. Koga, J. Phys. Soc. Jpn. **89**, 064002 (2020).
[27] N. Takemori, R. Arita, and S. Sakai, Phys. Rev. B **102**, 115108 (2020).
[28] A. Koga, Phys. Rev. B **102**, 115125 (2020).
[29] R. Ghadimi, T. Sugimoto, K. Tanaka, and T. Tohyama, Phys. Rev. B **104**, 144511 (2021).
[30] A. Koga, Mater. Trans. **62**, 360 (2021).
[31] S. Sakai and A. Koga, Mater. Trans. **62**, 380 (2021).
[32] K. Inayoshi, Y. Murakami, and A. Koga, Phys. Rev. B **105**, 104307 (2022).
[33] A. Koga and S. Coates, Phys. Rev. B **105**, 104410 (2022).
[34] P. Stampfli, Helv. Phys. Acta **59**, 1260 (1986).
[35] J. Hermisson, C. Richard, and M. Baake, J. Phys. I France **7**, 1003 (1997).
[36] J. Kim and S. Torquato, J. Stat. Mech. (2017) 013402.
[37] N. de Bruijn, Indag. Math. Proc. Ser. A **84**, 39 (1981).
[38] M. Gardner, Sci. Am. **236**, 110 (1977).
[39] M. Takano, Z. Hiroi, M. Azuma, and Y. Takeda, Jpn. J. Appl. Phys. **7**, 3 (1992).
[40] Z. Hiroi, M. Azuma, M. Takano, and Y. Bando, J. Solid State Chem. **95**, 230 (1991).
[41] H. Kageyama, K. Yoshimura, R. Stern, N. V. Mushnikov, K. Onizuka, M. Kato, K. Kosuge, C. P. Slichter, T. Goto, and Y. Ueda, Phys. Rev. Lett. **82**, 3168 (1999).
[42] S. Gopalan, T. M. Rice, and M. Sigrist, Phys. Rev. B **49**, 8901 (1994).
[43] B. Sriram Shastry and B. Sutherland, Physica B+C **108**, 1069 (1981).
[44] S. Miyahara and K. Ueda, Phys. Rev. Lett. **82**, 3701 (1999).
[45] A. Koga and N. Kawakami, Phys. Rev. Lett. **84**, 4461 (2000).
[46] N. Niizeki and H. Mitani, J. Phys. A **20**, L405 (1987).
[47] F. Gähler, *Quasicrystalline Materials* (World Scientific, Singapore, 1988).
[48] J. E. S. Socolar, Phys. Rev. B **39**, 10519 (1989).

[49] S. Förster, K. Meinel, R. Hammer, M. Trautmann, and W. Widdra, Nature (London) **502**, 215 (2013).
[50] S. Schenk, S. Förster, K. Meinel, R. Hammer, B. Leibundgut, M. Paleschke, J. Pantzer, C. Dresler, F. O. Schumann, and W. Widdra, J. Phys.: Condens. Matter **29**, 134002 (2017).
[51] T. Yamada, Acta Cryst. B **78**, 247 (2022).
[52] M. A. Keskiner and M. O. Oktel, Phys. Rev. B **106**, 064207 (2022).
[53] M. Baake and D. Joseph, Phys. Rev. B **42**, 8091 (1990).
[54] R. Lifshitz, J. Alloys Comp. **342**, 186 (2002).
[55] S. Coates, A. Koga, T. Matsubara, R. Tamura, H. R. Sharma, R. McGrath, and R. Lifshitz, arXiv:2201.11848.
[56] S. Torquato, M. Skolnick, and J. Kim, J. Phys. A: Math. Theor. **55**, 274003 (2022).
[57] Z. Ma and S. Torquato, J. Appl. Phys. **121**, 244904 (2017).